

\mathcal{PT} -assisted control of Goos-Hänchen shift in cavity magnomechanics

Shah Fahad¹ and Gao Xianlong^{1,*}

¹*Department of Physics, Zhejiang Normal University, Jinhua, Zhejiang 321004, China*

(Dated: November 26, 2025)

We propose a scheme to manipulate the Goos-Hänchen shift (GHS) of a reflected probe field in a non-Hermitian cavity magnomechanical system. The platform consists of a yttrium-iron-garnet sphere coupled to a microwave cavity, where a strong microwave drive pumps the magnon mode and a weak field probes the cavity. The traveling field's interaction with the magnon induces gain, yielding non-Hermitian dynamics. When the traveling field is oriented at $\pi/2$ relative to the cavity's x -axis, the system realizes \mathcal{PT} symmetry; eigenvalue analysis reveals a third-order exceptional point (EP₃) at a tunable effective magnon-photon coupling. Under balanced gain-loss and finite effective magnomechanical coupling, we demonstrate coherent control of the GHS by steering the system across the \mathcal{PT} -symmetric transition and through EP₃ via the effective magnon-photon coupling, enabling pronounced enhancement or suppression of the lateral shift. Furthermore, we show that without effective magnomechanical coupling, the system exhibits a second-order exceptional point (EP₂) with a distinct GHS phase transition. This phase transition vanishes when the effective magnomechanical coupling exceeds a parametric threshold, where strong absorption at resonance suppresses the GHS. We also identify the intracavity length as an additional control parameter for precise shift tuning. Notably, the \mathcal{PT} -symmetric configuration yields substantially larger GHS than its Hermitian counterpart. These results advance non-Hermitian magnomechanics and open a route to GHS-based microwave components for quantum switching and precision sensing.

I. INTRODUCTION

Magnons, the quantized spin excitations in magnetic materials [1], have emerged as a key platform for investigating macroscopic quantum phenomena [2–4]. By uniting magnons, photons, and phonons, cavity magnomechanics serves as a versatile testbed bridging quantum information science, magnonics, cavity quantum electrodynamics, and quantum optical studies [5]. This integrated framework enables the exploration of both semiclassical and quantum dynamics, leading to diverse applications such as ultrahigh-sensitivity sensing [6, 7], generation of squeezed and entangled states [8–12], ultraslow light [13, 14], and the transfer, storage, and retrieval of quantum states [15, 16]. Recent experiments have demonstrated fundamental phenomena such as magnomechanically induced absorption and transparency [17], along with advanced functionalities including mechanical bistability [18], magnonic frequency combs [19], and efficient microwave-optical transduction [18].

Non-Hermitian physics has emerged as a vibrant research field that explores systems governed by non-Hermitian Hamiltonians $H \neq H^\dagger$, whose complex eigenvalues reflect energy exchange with the environment [20, 21]. Mostafazadeh introduced pseudo-Hermiticity, wherein a non-Hermitian Hamiltonian H with a discrete spectrum satisfies $H^\dagger = \eta H \eta^{-1}$ for a linear Hermitian operator η , guaranteeing that its eigenvalues are either real or appear in complex-conjugate pairs [22, 23]. \mathcal{PT} -symmetric Hamiltonians, characterized by $[H, \mathcal{PT}] = 0$, constitute a significant sub-

set of pseudo-Hermitian systems [24–26] that can exhibit entirely real energy spectra under balanced gain and loss [27, 28]. Varying a control parameter drives the system through a second-order exceptional point (EP₂), triggering spontaneous \mathcal{PT} -symmetry breaking through the coalescence of eigenvalues and their corresponding eigenvectors. This bifurcation demarcates the transition from the unbroken \mathcal{PT} -symmetric phase (real spectrum) to the broken \mathcal{PT} phase (complex-conjugate spectrum) [29–31]. EP₂s have been rigorously investigated across diverse physical systems, revealing phenomena such as topological energy transfer [32], loss-induced lasing revival [33], enhanced sensitivity [34], coherent absorption [35, 36], single-mode lasing [37, 38], and optimized energy harvesting [39]. Beyond EP₂, higher-order exceptional points (EP_n, $n > 2$) exhibit stronger non-Hermitian degeneracies where n eigenstates coalesce [25, 26, 40–43]. These higher-order EPs enable greater sensitivity [44, 45], enhanced spontaneous emission [46], rapid entanglement generation [47] and richer topological features [48, 49]. Recent advances demonstrate sophisticated control over phenomena such as microwave field transmission using engineered non-Hermitian systems [4, 50]. In this work, we investigate the physics of EP₃ on Goos-Hänchen shift (GHS) as a distinct and measurable signature of the optical response in a \mathcal{PT} -symmetric non-Hermitian cavity magnomechanical (CMM) system.

The GHS is an optical phenomenon governing the lateral shift (parallel to the plane of incidence) of light beams at interfaces between media structures [51–54]. This shift originates from spatial dispersion in transverse magnetic (TM) or transverse electric (TE) reflection coefficients and interference among angular spectrum components (i.e., phase variations in reflection co-

* gaoxl@zjnu.edu.cn

efficients) [53, 55, 56]. The GHS was first theoretically predicted by Picht [57], experimentally verified by Goos and Hänchen [58, 59], and later rigorously formalized by Artmann via the stationary-phase method [60]. The GHS magnitude's sign (positive/negative) emerges from the system's parameter-dependent phase response [61, 62]. The GHS has been extensively explored and manipulated in numerous quantum systems, including quantum dots [63], atom-cavity quantum electrodynamics (QED) setups [54], and cavity optomechanical platforms [64, 65]. Its applications span multiple domains, such as quantum sensing [66], neutron optics [67, 68], temperature measurement [69], and humidity sensing [70]. More recently, the GHS has been investigated within a Hermitian CMM system [71]. However, the evolution of the GHS in \mathcal{PT} -symmetric CMM systems—particularly across their phase transitions and at a third-order exceptional point (EP₃)—remains uncharacterized. Here, we analyze a hybrid three-mode system featuring the coherent interplay of photon–magnon and magnon–phonon couplings. Under experimentally feasible parameters, we demonstrate that these interactions govern the lateral shift, yielding a phase-selective response. The GHS exhibits pronounced enhancement or suppression at the EP₃ and across the \mathcal{PT} phases, governed by the system's non-Hermitian eigenvalue structure. Our results establish coherent control over the GHS in a non-Hermitian CMM system, presenting a novel paradigm for tunable microwave devices and enhanced sensing.

We consider a non-Hermitian CMM system that spans the broken \mathcal{PT} phase, EP₃, and the unbroken \mathcal{PT} phase. The system comprises a microwave cavity with two fixed mirrors and an embedded yttrium iron garnet (YIG) sphere. A z -axis bias magnetic field B_z excites the magnon modes in the YIG sphere, coupling to cavity photons through magnetic dipole interactions, while magnetostrictive interactions mediate the magnon–phonon coupling via lattice deformation. Non-Hermiticity is introduced through a traveling field driving the magnon mode, inducing gain. Under gain-loss balance conditions and finite effective magnomechanical coupling, an EP₃ emerges when the effective magnon–photon coupling strength is tuned to a critical value.

Using the stationary-phase method, we then systematically analyze the GHS in the reflected probe field across the different \mathcal{PT} -symmetric phases. Our results reveal strong phase-dependent behavior: the GHS is significantly enhanced in the unbroken \mathcal{PT} phase compared to the broken phase, consistent with the previous report of enhanced beam shifts in atomic-ensemble-based \mathcal{PT} -symmetric cavity [52]. In contrast, the EP₃ regime exhibits a suppressed GHS. We further demonstrate that the GHS can be actively controlled across \mathcal{PT} phases by tuning the intracavity length. Finally, a direct comparison under identical parameters shows that the GHS in the \mathcal{PT} -symmetric system exceeds that of the corresponding Hermitian configuration [71], highlighting the enhanced phase sensitivity enabled by the gain–loss balance.

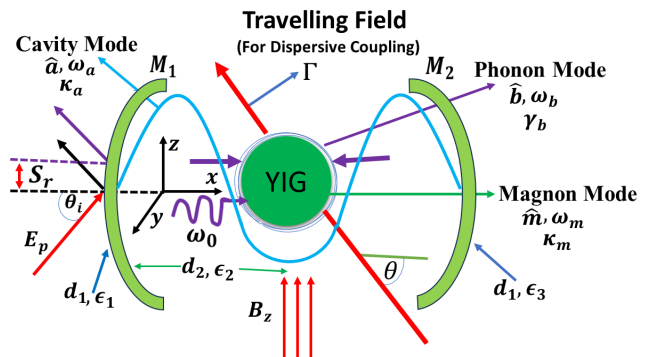


FIG. 1. Schematic illustration of a non-Hermitian CMM system featuring an embedded YIG sphere. The cavity mode (\hat{a} with frequency ω_a and dissipation rate κ_a) is subjected to a bias magnetic field B_z along the z -axis, which excites the magnon mode (\hat{m} with frequency ω_m and gain κ_m). Magnon–photon coupling arises from magnetic dipole interactions. Magnetostrictive interactions induce the phonon mode (\hat{b} with frequency ω_b and dissipation rate γ_b), facilitating magnon–phonon coupling that is further enhanced by an x -axis microwave drive field (frequency ω_0). The perpendicular magnetic fields—cavity (B_y), drive (B_x), and bias (B_z)—are depicted. Non-Hermiticity emerges from a traveling field characterized by incident angle θ and coupling strength Γ . A TE-polarized probe field E_p is incident on mirror M_1 at angle θ_i . The lateral displacement experienced by the reflected probe field during total internal reflection constitutes the GHS, denoted by S_r .

The rest of the manuscript is structured as follows: Section II introduces the system Hamiltonian. We derive the optical susceptibility using the semiclassical Heisenberg–Langevin equations and then employ the stationary-phase method to calculate the GHS of the reflected probe field. Sec. III presents the results and discussion, focusing on the output field spectra and the control of the GHS via the system's parameters. Sec. IV concludes.

II. THEORETICAL MODEL

A. System Hamiltonian

We consider a hybrid non-Hermitian CMM system comprising a single-mode cavity (\hat{a} , frequency ω_a) with an embedded YIG sphere, as shown in Fig. 1. The YIG sphere is positioned at an antinode of the cavity's microwave magnetic field to optimize magnon–photon coupling. The setup includes two nonmagnetic mirrors (M_1 and M_2) separated by a fixed distance d_2 . M_2 is perfectly reflective, while M_1 is partially reflective. Both mirrors have identical thickness d_1 and permittivities ϵ_1 and ϵ_3 , respectively, while the intracavity medium is characterized by an effective permittivity ϵ_2 . This three-layer configuration is analogous to cavity optomechanics [64] and atomic systems [55]. A uniform bias magnetic field B_z applied along the z -axis excites magnon modes

(\hat{m} , frequency ω_m) in the YIG sphere. These magnon modes couple with the cavity photon modes via magnetic dipole interaction. The magnetization dynamics induced by the magnon excitation lead to lattice deformation through magnetostriiction, giving rise to phonon modes (\hat{b} , frequency ω_b). Consequently, magnon-phonon coupling arises from the magnetostriuctive interaction. The magnon mode is driven by microwave field (frequency ω_0 , amplitude $\eta = \sqrt{5N\gamma B_0}/4$, with external magnetic field B_0 , total spins N , and gyromagnetic ratio γ). A weak probe field, with amplitude $E_p = \sqrt{2P\kappa_a/\hbar\omega_p}$ (corresponding to power P , frequency ω_p , and incident angle θ_i), drives the cavity mode. The non-Hermitian behavior of the system arises from the direct interaction with a traveling field, which introduces gain in the magnon mode (with mass m_m and frequency ω_m), characterized by a coupling strength $\Gamma = \frac{\omega_a}{d_2} \sqrt{\hbar/\omega_m m_m}$ [72–74].

Under the rotating-wave approximation, the total Hamiltonian in a frame rotating at the drive frequency ω_0 becomes [75]:

$$\begin{aligned} \hat{\mathcal{H}} = & \hbar\Delta_a\hat{a}^\dagger\hat{a} + \hbar\Delta_m\hat{m}^\dagger\hat{m} + \hbar\omega_b\hat{b}^\dagger\hat{b} \\ & + \hbar(g_{ma} - i\Gamma e^{i\theta})(\hat{a}\hat{m}^\dagger + \hat{a}^\dagger\hat{m}) + \hbar g_{mb}\hat{m}^\dagger\hat{m}(\hat{b}^\dagger + \hat{b}) \\ & + i\hbar\eta(\hat{m}^\dagger - \hat{m}) + i\hbar E_p(\hat{a}^\dagger e^{-i\Delta_p t} - \hat{a} e^{i\Delta_p t}). \end{aligned} \quad (1)$$

Here $\Delta_a = \omega_a - \omega_0$, $\Delta_m = \omega_m - \omega_0$, and $\Delta_p = \omega_p - \omega_0$. \hat{a} , \hat{b} , \hat{m} (\hat{a}^\dagger , \hat{b}^\dagger , \hat{m}^\dagger) are annihilation (creation) operators; g_{ma} (g_{mb}) is the magnon-photon (magnon-phonon) coupling.

We derive the semiclassical Heisenberg-Langevin equations for the operators $\hat{O} \in \{\hat{a}, \hat{m}, \hat{b}\}$ to describe the average cavity response, neglecting both thermal and quantum noise:

$$\frac{d\hat{O}}{dt} = \frac{i}{\hbar} [\hat{\mathcal{H}}, \hat{O}] - \beta\hat{O}, \quad (2)$$

where β represents the gain ($\beta < 0$) or decay rate ($\beta > 0$). The canonical commutation relation $[\hat{O}, \hat{O}^\dagger] = 1$ holds for $\hat{O} \in \{\hat{a}, \hat{m}, \hat{b}\}$. Replacing the operators with their expectation values, $O(t) \equiv \langle \hat{O}(t) \rangle$ ($O = a, m, b$) [76], yields:

$$\begin{aligned} \dot{a} = & -(i\Delta_a + \kappa_a)a - (ig_{ma} + \Gamma e^{i\theta})m + E_p e^{-i\Delta_p t}, \\ \dot{m} = & -(i\Delta_m - \kappa_m)m - (ig_{ma} + \Gamma e^{i\theta})a - ig_{mb}m(b^* + b) + \eta, \\ \dot{b} = & -(i\omega_b + \gamma_b)b - ig_{mb}m^*m. \end{aligned} \quad (3)$$

Here κ_a (γ_b) is the photon (phonon) dissipation rate, and κ_m the magnon gain. The steady-state solutions are:

$$\begin{aligned} a_s = & \frac{-(ig_{ma} + \Gamma e^{i\theta})m_s}{(i\Delta_a + \kappa_a)}, \\ m_s = & \frac{-(ig_{ma} + \Gamma e^{i\theta})a_s + \eta}{(i\Delta_m - \kappa_m)}, \\ b_s = & \frac{-ig_{mb}|m_s|^2}{(i\omega_b + \gamma_b)}, \end{aligned} \quad (4)$$

where $\Delta_s = \Delta_m + g_{mb}(b_s^* + b_s)$ is the effective magnon-phonon detuning. After linearizing Eq. (3) and retaining the first-order terms, we obtain:

$$\begin{aligned} \delta\dot{a} = & -(i\Delta_a + \kappa_a)\delta a - (ig_{ma} + \Gamma e^{i\theta})\delta m + E_p e^{-i\Delta_p t}, \\ \delta\dot{m} = & -(i\Delta_s - \kappa_m)\delta m - (ig_{ma} + \Gamma e^{i\theta})\delta a - ig_{mb}m_s\delta b, \\ \delta\dot{b} = & -(i\omega_b + \gamma_b)\delta b - ig_{mb}m_s^*\delta m. \end{aligned} \quad (5)$$

B. Exceptional point and \mathcal{PT} -symmetry

The first-order linearized Heisenberg-Langevin equations in Eq. (5) can be written in the following matrix form:

$$\dot{\mathbf{X}} = -iH_{\text{eff}}\mathbf{X}, \quad (6)$$

where $\mathbf{X} = (\delta a, \delta m, \delta b)^\top$ denotes the column vector of dynamical variables, and H_{eff} corresponds to the effective non-Hermitian Hamiltonian governing the hybrid system,

$$H_{\text{eff}} = \begin{pmatrix} \Delta_a - i\kappa_a & g_{ma} - i\Gamma e^{i\theta} & 0 \\ g_{ma} - i\Gamma e^{i\theta} & \Delta_s + i\kappa_m & G_b \\ 0 & G_b^* & \omega_b - i\gamma_b \end{pmatrix}, \quad (7)$$

where $G_b = g_{mb}m_s$ is the effective magnon-phonon (magnomechanical) coupling coefficient. This hybrid three-mode system with magnon-photon and magnon-phonon couplings yields three eigenvalues. The eigenvalues λ are determined by the characteristic equation:

$$\lambda^3 + r\lambda^2 + s\lambda + t = 0, \quad (8)$$

where $r = -[\Delta_a - i\kappa_a + \Delta_s + i\kappa_m + \omega_b - i\gamma_b]$, $s = (\Delta_a - i\kappa_a)(\Delta_s + i\kappa_m + \omega_b - i\gamma_b) + (\Delta_s + i\kappa_m)(\omega_b - i\gamma_b) - |G_b|^2 - (g_{ma} - i\Gamma e^{i\theta})^2$, $t = -(\Delta_a - i\kappa_a)(\Delta_s + i\kappa_m)(\omega_b - i\gamma_b) + |G_b|^2(\Delta_a - i\kappa_a) + (\omega_b - i\gamma_b)(g_{ma} - i\Gamma e^{i\theta})^2$.

Based on the effective Hamiltonian in Eq. (7), the \mathcal{PT} -symmetric phases of the system were rigorously analyzed in Ref. [75] (Fig. 2). In this work, we investigate the GHS behavior that emerges across these \mathcal{PT} -symmetric regimes and at the EP₃.

C. Optical Susceptibility

To evaluate the optical susceptibility of the coupled system, we solve Eq. (5) by introducing the slowly varying operators for the linear fluctuation terms: $\delta a \rightarrow \delta a e^{-i\Delta_a t}$, $\delta m \rightarrow \delta m e^{-i\Delta_m t}$, and $\delta b \rightarrow \delta b e^{-i\omega_b t}$. We then apply the ansatz $\delta O = \delta O_1 e^{-ixt} + \delta O_2 e^{ixt}$ with $O = (a, m, b)$ and the effective detuning $x = \Delta_p - \omega_b$. This approach yields an explicit expression for the amplitude δa_1 of the first-order sideband in the non-Hermitian CMM system for a weak probe field:

$$\delta a_1 = \frac{E_p}{(\kappa_a - ix) + \frac{(\gamma_b - ix)(ig_{ma} + \Gamma e^{i\theta})^2}{(\kappa_m + ix)(\gamma_b - ix) - |G_b|^2}}. \quad (9)$$

The contribution of δa_2 is negligible, as it stems from a four-wave mixing process at frequency $\omega_p - 2\omega_0$ between the weak probe and the driving fields. The output field E_T of the weak probe field defines the optical susceptibility χ via the relation [71, 77–79]

$$\chi \equiv E_T = \kappa_a \delta a_1 / E_p, \quad (10)$$

where χ is a complex quantity, expressed in terms of its quadrature components as $\chi = \chi_r + i\chi_i$. These components are measured via homodyne detection [80]. The real (χ_r) and imaginary (χ_i) components of the χ describe the absorption and dispersion spectra of the probe field, respectively.

D. Goos-Hänchen shift

The TE-polarized probe field E_p reflects from mirror M_1 , resulting in a lateral displacement (GHS) S_r along the z -axis. We employ the stationary phase method to quantify this displacement. Within this framework, the well-collimated probe field—with sufficiently narrow angular divergence—can be approximated as a plane wave. The GHS of the reflected probe field is then expressed as [60, 61]

$$S_r = -\frac{\lambda_p}{2\pi} \frac{d\phi_r}{d\theta_i}, \quad (11)$$

where λ_p is the incident probe field wavelength, ϕ_r is the phase of the TE-polarized reflection coefficient $r(k_z, \omega_p)$,

$k_z = (2\pi/\lambda_p) \sin \theta_i$ is the z -component of the wavenumber, and θ_i is the probe field incidence angle. The GHS takes the explicit form [55, 81]

$$S_r = -\frac{\lambda_p}{2\pi} \frac{1}{|r(k_z, \omega_p)|^2} \left\{ \text{Re}[r(k_z, \omega_p)] \frac{d \text{Im}[r(k_z, \omega_p)]}{d\theta_i} \right. \\ \left. - \text{Im}[r(k_z, \omega_p)] \frac{d \text{Re}[r(k_z, \omega_p)]}{d\theta_i} \right\}. \quad (12)$$

The reflection coefficient $r(k_z, \omega_p)$ used in Eq. (12) is obtained using the standard transfer-matrix method for the j -th layer system [55]

$$M_j(k_z, \omega_p, d_j) = \begin{pmatrix} \cos[k_x^j d_j] & ik/k_x^j \sin[k_x^j d_j] \\ ik_x^j/k \sin[k_x^j d_j] & \cos[k_x^j d_j] \end{pmatrix}, \quad (13)$$

where $k_x^j = k\sqrt{\varepsilon_j - \sin^2 \theta_i}$ is the x -component of the wavenumber of the probe field in the j -th layer. Here, $k = \omega_p/c$ is the wavenumber in vacuum, where c is the speed of light. For each layer ($j \equiv 1, 2, 3$), ε_j and d_j denote the permittivity and thickness, respectively. The effective intracavity permittivity $\varepsilon_2 = 1 + \chi$ emerges from the nonlinear optical susceptibility χ [Eq. 10]. The total transfer matrix for the effective three-layer system is expressed as [55]

$$Q(k_z, \omega_p) = M_1(k_z, \omega_p, d_1) M_2(k_z, \omega_p, d_2) M_1(k_z, \omega_p, d_1) = \begin{pmatrix} Q_{11} & Q_{12} \\ Q_{21} & Q_{22} \end{pmatrix}, \quad (14)$$

where $M_j(k_z, \omega_p, d_j)$ depends on the parameters of the corresponding layer. The reflection coefficient $r(k_z, \omega_p)$ is given by

$$r(k_z, \omega_p) = \frac{q_0(Q_{22} - Q_{11}) - (q_0^2 Q_{12} - Q_{21})}{q_0(Q_{22} + Q_{11}) - (q_0^2 Q_{12} + Q_{21})}, \quad (15)$$

where $q_0 = \sqrt{\varepsilon_0 - \sin^2 \theta_i}$, and Q_{ij} (with $i, j = 1, 2$) denote the elements of the transfer matrix $Q(k_z, \omega_p)$.

III. RESULTS AND DISCUSSION

In this section, we present numerical results using experimentally feasible parameters [17, 82]: cavity frequency $\omega_a/2\pi = 13.2$ GHz, mechanical frequency $\omega_b/2\pi = 15.101$ MHz, cavity decay rate $\kappa_a/2\pi = 2.1$ MHz, mechanical damping rate $\gamma_b/2\pi = 150$ Hz, magnon gain rate $\kappa_m = \kappa_a + \gamma_b$, and effective magnomechanical coupling coefficient $G_b/2\pi = 0.001$ MHz. The

YIG sphere (diameter $D = 250$ μm , spin density $\rho = 4.22 \times 10^{27}$ m^{-3} , gyromagnetic ratio $\gamma/2\pi = 28$ GHz/T) is driven by a magnetic field $B_0 \leq 0.5$ mT, yielding $G_b/2\pi \leq 1.5$ MHz [83]. For the GHS investigation, the dielectric constants are set to $\epsilon_0 = 1$, $\epsilon_1 = \epsilon_3 = 2.2$, with layer thicknesses $d_1 = 4$ mm and $d_2 = 45$ mm [17, 84]. The system exhibits \mathcal{PT} -symmetry exclusively when the angle between the traveling field and the cavity's x -axis is $\pi/2$.

Under balanced gain and loss conditions ($\kappa_m = \kappa_a + \gamma_b$) and with a finite effective magnomechanical coupling G_b , the eigenvalue spectrum of the non-Hermitian CMM system exhibits a \mathcal{PT} -symmetry phase transition, as described by Eq. (7) and detailed in Ref. [75] (Fig. 2). This transition is tuned by the effective magnon–photon coupling strength G_a . For $G_a/\omega_b < 0.139$, the system resides in the broken \mathcal{PT} -symmetric phase, characterized by complex eigenvalues. At the critical coupling $G_a/\omega_b = 0.139$, an EP₃ emerges, where both eigenval-

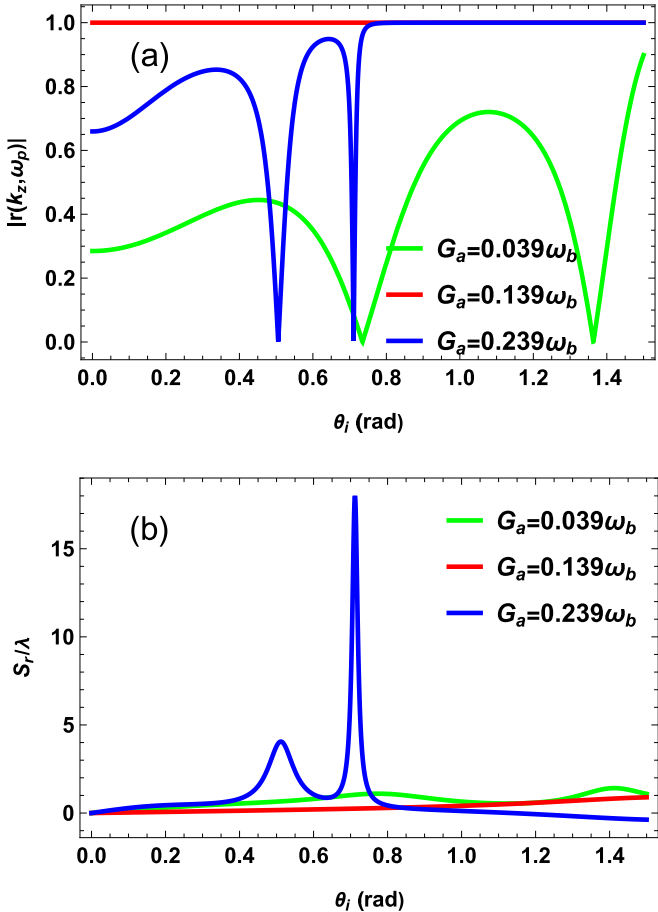


FIG. 2. (a) Absolute value of the reflection coefficient $|r(k_z, \omega_p)|$ and (b) the normalized GHS S_r/λ versus incident angle θ_i for three effective magnon-photon coupling regimes: (i) $G_a = 0.039\omega_b$ (green, broken \mathcal{PT} phase), (ii) $0.139\omega_b$ (red, third-order exceptional point EP₃), and (iii) $0.239\omega_b$ (blue, unbroken \mathcal{PT} phase) at the resonance condition ($x = 0$). Fixed parameters: $\omega_a/2\pi = 13.2$ GHz, $\kappa_a/2\pi = 2.1$ MHz, $\gamma_b/2\pi = 150$ Hz, $\kappa_m = \kappa_a + \gamma_b$, $\omega_b/2\pi = 15.101$ MHz, $G_b/2\pi = 0.001$ MHz, $\epsilon_0 = 1$, $\epsilon_1 = \epsilon_3 = 2.2$, $d_1 = 4$ mm, and $d_2 = 45$ mm.

ues and eigenvectors coalesce. When $G_a/\omega_b > 0.139$, the eigenvalue spectrum becomes entirely real, indicating the unbroken \mathcal{PT} -symmetric phase. Thus, the numerical analysis of the GHS is systematically delineated across three regimes: (i) broken \mathcal{PT} -symmetric phase, (ii) EP₃, and (iii) unbroken \mathcal{PT} -symmetric phase.

Equation (12) shows that the normalized GHS S_r/λ , depends on the reflection coefficient $|r(k_z, \omega_p)|$ of the incident TE-polarized probe field. Figures 2(a) and (b) display both $|r(k_z, \omega_p)|$ and S_r/λ as functions of the probe field incident angle θ_i for broken \mathcal{PT} phase (green), EP₃ (red), and unbroken \mathcal{PT} phase (blue). Figure 2(a) shows distinct reflection dips at specific incident angles of the probe field, corresponding to resonance conditions in both broken and unbroken \mathcal{PT} phases. These resonant features indicate the existence of lateral shifts in both phases. The GHS peaks in broken and unbro-

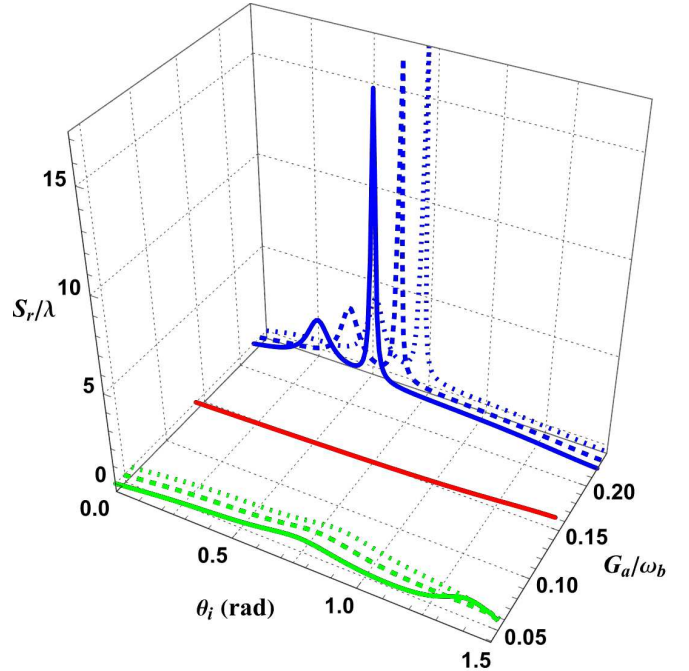


FIG. 3. Normalized GHS S_r/λ as a function of the incident angle θ_i , parametrized by the effective magnon-photon coupling strength G_a . The curves are shown for the three dynamical phases: broken \mathcal{PT} phase, EP₃, and the unbroken \mathcal{PT} phase, respectively, at resonance ($x = 0$). The effective coupling strengths are: $G_a/\omega_b = 0.039, 0.049, 0.058$ (green solid/dashed/dotted for the broken \mathcal{PT} phase); 0.139 (red solid at the EP₃); and $0.22, 0.229, 0.239$ (blue solid/dashed/dotted for the unbroken \mathcal{PT} phase). Fixed parameters are: $\omega_a/2\pi = 13.2$ GHz, $\omega_b/2\pi = 15.101$ MHz, $\kappa_a/2\pi = 2.1$ MHz, $\gamma_b/2\pi = 150$ Hz, $\kappa_m = \kappa_a + \gamma_b$, $G_b/2\pi = 0.001$ MHz, $\epsilon_0 = 1$, $\epsilon_1 = \epsilon_3 = 2.2$, $d_1 = 4$ mm, and $d_2 = 45$ mm.

ken \mathcal{PT} phases coincide with the reflection resonances of the probe field [Fig. 2(b)]. In the unbroken \mathcal{PT} phase, the GHS is significantly enhanced, exhibiting a large positive shift. In contrast, the broken \mathcal{PT} phase yields much smaller positive shifts across the entire angular range. This difference originates from the strong effective magnon-photon coupling in the unbroken \mathcal{PT} phase, which yields sharper reflection resonances and steeper phase gradients, thereby amplifying the GHS. The observed GHS enhancement agrees with previous reports for atomic-ensemble-based \mathcal{PT} -symmetric cavities [52]. On the other hand, the weaker effective coupling in the broken phase leads to broader spectral features and reduced phase dispersion, thus suppressing the shift [Fig. 2(b)]. At the EP₃, the coalescence of eigenvalues and their corresponding eigenvectors flattens the reflection phase ($|r(k_z, \omega_p)| \approx 1$), eliminating phase dispersion and causing the GHS to approach zero.

In Figs. 2(a) and (b), we analyze representative values of the effective magnon-photon coupling strength G_a corresponding to the broken \mathcal{PT} phase, EP₃, and the unbroken \mathcal{PT} phase. To generalize these results, we ex-

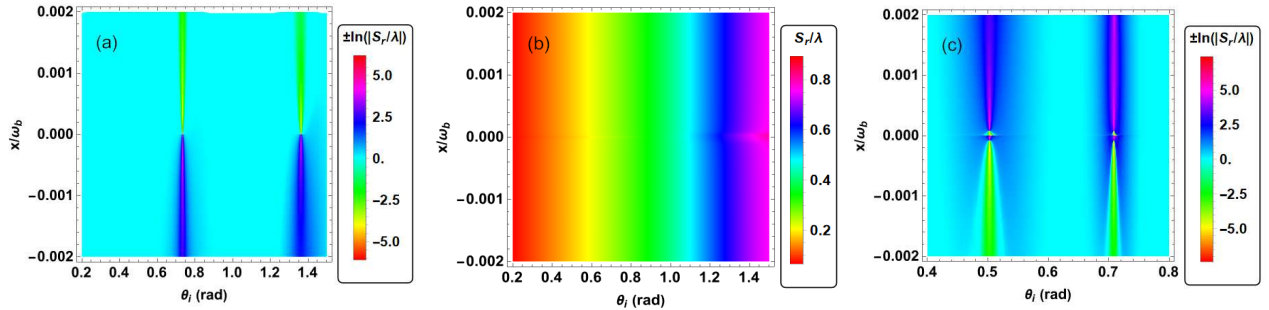


FIG. 4. Contour plots of normalized GHS S_r/λ versus incident angle θ_i and normalized effective detuning x/ω_b for: (a) broken \mathcal{PT} phase ($G_a = 0.039 \omega_b$), (b) EP₃ ($G_a = 0.139 \omega_b$), and (c) unbroken \mathcal{PT} phase ($G_a = 0.239 \omega_b$). Fixed parameters: $\omega_a/2\pi = 13.2$ GHz, $\omega_b/2\pi = 15.101$ MHz, $\kappa_a/2\pi = 2.1$ MHz, $\gamma_b/2\pi = 150$ Hz, $\kappa_m = \kappa_a + \gamma_b$, $G_b/2\pi = 0.001$ MHz, $\epsilon_0 = 1$, $\epsilon_1 = \epsilon_3 = 2.2$, $d_1 = 4$ mm, and $d_2 = 45$ mm.

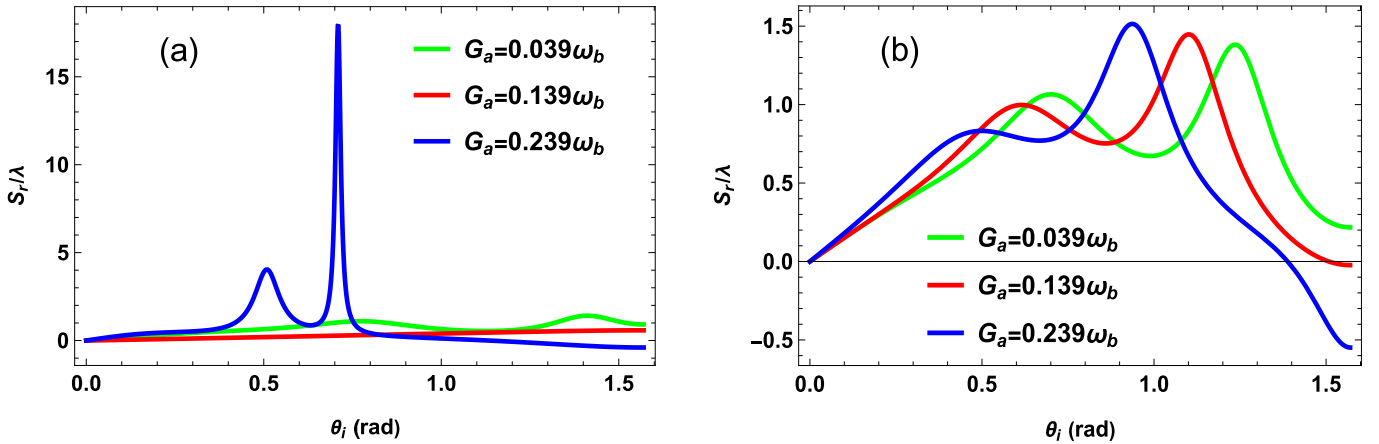


FIG. 5. Normalized GHS S_r/λ versus incident angle θ_i for two cases: (a) $G_b = 0$ and (b) $G_b/2\pi = 0.05$ MHz at resonance ($x = 0$). Fixed parameters: $G_a = 0.039 \omega_b$ (broken \mathcal{PT} phase, green), $G_a = 0.139 \omega_b$ (EP₂, red), $G_a = 0.239 \omega_b$ (unbroken \mathcal{PT} phase, blue), $\omega_a/2\pi = 13.2$ GHz, $\kappa_a/2\pi = 2.1$ MHz, $\gamma_b/2\pi = 150$ Hz, $\kappa_m = \kappa_a + \gamma_b$, $\omega_b/2\pi = 15.101$ MHz, $\epsilon_0 = 1$, $\epsilon_1 = \epsilon_3 = 2.2$, $d_1 = 4$ mm, and $d_2 = 45$ mm.

plore a broader range of G_a within each regime and observe consistent qualitative behavior: the GHS is significantly enhanced in the unbroken \mathcal{PT} phase, strongly suppressed in the broken phase, and approaches zero at the EP₃ [Fig. 3]. The angular dependence and magnitude of the GHS in each regime are governed by G_a , illustrating tunable control over this lateral shift. This reproducibility across the parameter space highlights the robustness of the results and emphasizes the central role of \mathcal{PT} -symmetry in modulating the GHS.

Next, we analyze the contour plots of the GHS S_r/λ as a function of both the incident angle θ_i and the normalized effective detuning x/ω_b . Figures 4(a-c) show the S_r/λ versus θ_i and x/ω_b in the broken \mathcal{PT} phase, EP₃, and unbroken \mathcal{PT} phase, respectively. For the broken and unbroken \mathcal{PT} phases, we employed a minimal step size (for both variables) to generate smooth, high-resolution plots [Figs. 4(a) and (b)]. Consequently, some peaks and dips appear sharply defined with large amplitudes. In the broken \mathcal{PT} phase [Fig. 4(a)], weak effective magnon–photon coupling produces complex eigenvalues, leading to asymmetric GHS. This results in a positive

lateral shift for negative cavity detunings and a negative shift for positive detunings. At the EP₃ [Fig. 4(b)], the coalescence of eigenvalues and eigenvectors flattens the reflection phase, thereby suppressing the GHS. In contrast, the unbroken \mathcal{PT} phase [Fig. 4(c)] exhibits real eigenvalues and a sharp, symmetric GHS enabled by strong, coherent effective magnon-photon coupling, where the shift manifests as symmetric bands of large positive and negative lateral displacements centered at resonance ($x = 0$).

Figures 5(a) and (b) illustrate the normalized GHS S_r/λ as a function of the probe field's incident angle θ_i for different effective magnomechanical coupling coefficients G_b . For $G_b = 0$, the system exhibits a distinct phase transition in the GHS [Fig. 5(a)], consistent with the \mathcal{PT} -symmetric eigenvalue spectrum characteristic of an EP₂ system [75] (Fig. 3). In contrast, at $G_b = 2\pi \times 0.05$ MHz, the effective magnomechanical interaction significantly suppresses the overall GHS, eliminating the phase transition while concurrently enhancing the magnitude of the negative shift at higher incident angles [Fig. 5(b)]. This suppression is attributed to increased absorption of the

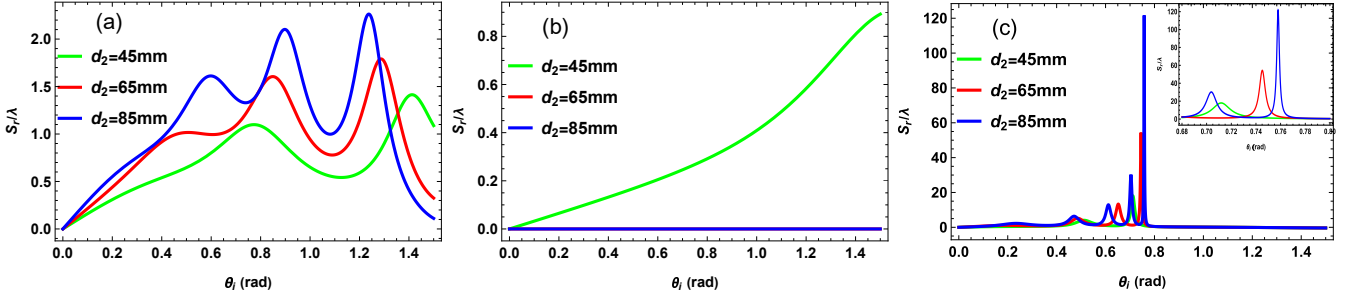


FIG. 6. Normalized GHS S_r/λ as a function of incident angle θ_i for (a) broken \mathcal{PT} phase ($G_a = 0.039\omega_b$), (b) EP₃ ($G_a = 0.139\omega_b$), and (c) unbroken \mathcal{PT} phase ($G_a = 0.239\omega_b$), respectively at three different intracavity medium lengths. Green, red, and blue curves show the GHS at $d_2 = 45$, 65, and 85 mm, respectively, at the resonance condition ($x = 0$). The insets in Fig. 6(c) provide magnified views of S_r/λ as a function of θ_i in \mathcal{PT} -symmetric phase at different intracavity medium lengths. Fixed parameters are $\kappa_a/2\pi = 2.1$ MHz, $\gamma_b/2\pi = 150$ Hz, $\kappa_m = \kappa_a + \gamma_b$, $\omega_b/2\pi = 15.101$ MHz, $G_b/2\pi = 0.001$ MHz, $\omega_a/2\pi = 13.2$ GHz, $d_1 = 4$ mm, $\epsilon_0 = 1$, and $\epsilon_1 = \epsilon_3 = 2.2$.

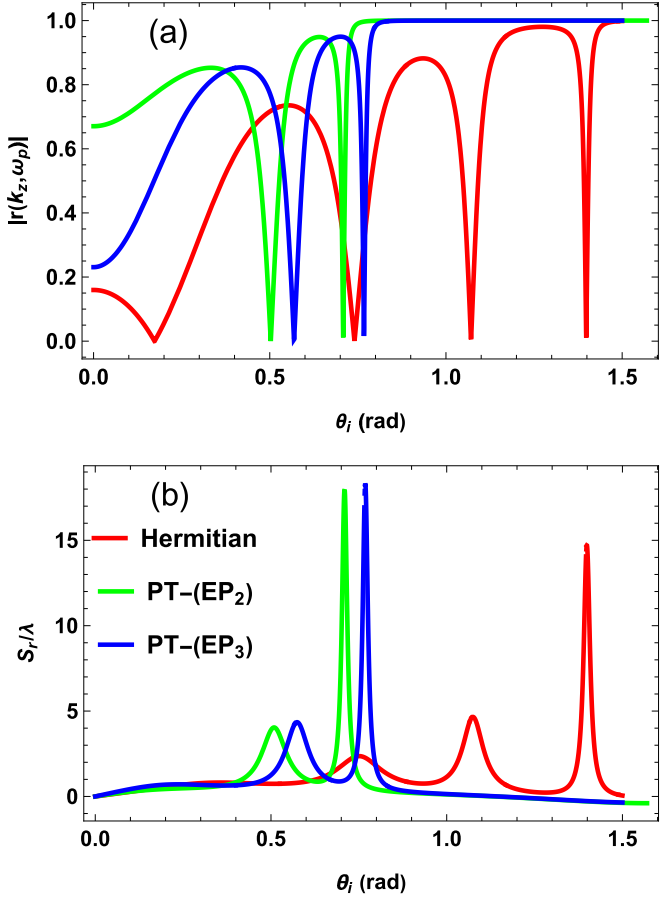


FIG. 7. (a) Reflection coefficient $|r(k_z, \omega_p)|$ and (b) the normalized GHS S_r/λ versus incident angle θ_i for Hermitian case ($G_b/2\pi = 0.005$ MHz, red curves, $\kappa_m/2\pi = 0.1$ MHz), and \mathcal{PT} -symmetric system ($G_b = 0$, EP₂, green curves, and $G_b/2\pi = 0.005$ MHz, EP₃, blue curves, $\kappa_m = \kappa_a + \gamma_b$) at the resonance condition ($x = 0$). Fixed parameters: $G_a = 0.239\omega_b$, $\omega_a/2\pi = 13.2$ GHz, $\kappa_a/2\pi = 2.1$ MHz, $\gamma_b/2\pi = 150$ Hz, $\omega_b/2\pi = 15.101$ MHz, $\epsilon_0 = 1$, $\epsilon_1 = \epsilon_3 = 2.2$, $d_1 = 4$ mm, and $d_2 = 45$ mm.

probe field at higher G_b [71]. Furthermore, the transition of the GHS from positive to negative is associated with the group index of the overall cavity system [54, 71].

The GHS S_r/λ depends crucially on the cavity geometry, particularly the total thickness $L = 2d_1 + d_2$, which necessitates precise dimensional control. Figures 6(a-c) show S_r/λ versus the incident angle θ_i at resonance ($x = 0$) for intracavity lengths of $d_2 = 45$ mm, 65 mm, and 85 mm. In the broken \mathcal{PT} phase, both the GHS magnitude and the number of resonant peaks increase with d_2 [Fig. 6(a)]. At the EP₃ [Fig. 6(b)], the GHS is suppressed and approaches zero as d_2 increases. While the unbroken \mathcal{PT} phase exhibits enhanced GHS magnitudes and a stronger dependence on d_2 than its broken phase [Fig. 6(c)]. This intracavity length-dependent behavior in non-Hermitian cavity magnomechanics is analogous to the earlier observations in atomic systems [54] and Hermitian cavity magnomechanics [71], confirming the importance of cavity dimensions for controlling the GHS.

Finally, we compare the reflection coefficient magnitude $|r(k_z, \omega_p)|$ and the normalized GHS S_r/λ for both Hermitian and \mathcal{PT} -symmetric systems containing EP₂ and EP₃. The Hermitian case, corresponding to $\Gamma = 0$ in Eq. (1), reproduces the optical susceptibility described in Ref. [71]. Figures 7(a) and (b), which show $|r(k_z, \omega_p)|$ and S_r/λ respectively, indicate that the \mathcal{PT} -symmetric system—encompassing both EP₂ (green) and EP₃ (blue)—exhibits a pronounced enhancement of the GHS relative to the Hermitian case (red). This enhancement arises from the gain-loss balance, which increases the reflection-phase sensitivity. As a result, the \mathcal{PT} -symmetric configuration provides greater control over the amplitude and phase of the reflected probe field, producing larger GHS [Fig. 7(b)] than those achieved in Hermitian systems [71]. Moreover, the shift associated with EP₃ is comparatively larger than that at EP₂, reflecting stronger phase sensitivity in higher-order EP systems. These results underscore the advantages of \mathcal{PT} -symmetric structures for applications demanding precise

angular control and selective signal routing, outperforming conventional photonic systems.

IV. CONCLUSION

In summary, we have investigated the GHS of a reflected probe field in a hybrid non-Hermitian CMM system. The system exhibits three distinct phases—(a) broken \mathcal{PT} symmetry, (b) third-order exceptional point EP_3 , and (c) unbroken \mathcal{PT} symmetry, which collectively establish a controlled platform for exploring phase-dependent lateral-shift phenomena.

Analysis at resonance ($x = 0$) revealed that the GHS magnitude was substantially enhanced in the unbroken \mathcal{PT} phase compared to the broken \mathcal{PT} phase, consistent with previous findings [52]. In contrast, at the EP_3 —characterized by the coalescence of eigenvalues and eigenvectors—the GHS demonstrated strong suppression. This qualitative behavior is consistent across a broad range of effective magnon-photon coupling, with the GHS remaining enhanced in the unbroken phase, suppressed in the broken phase, and vanishing at the EP_3 . Furthermore, we have shown that the effective magnomechanical coupling is a critical parameter: in its absence, the system exhibits an EP_2 , and the GHS undergoes a clear phase transition. However, when this effective magnomechanical coupling is increased beyond a parametric window, the phase transition disappears, and

strong absorption emerges at resonance, leading to a decrease in the magnitude of the GHS. Using the intracavity length as an active tuning parameter, we further demonstrate that the GHS increases with intracavity length in both the broken and unbroken \mathcal{PT} phases—though with markedly different magnitudes—while remaining suppressed at the EP_3 . Comparative analysis between \mathcal{PT} -symmetric and Hermitian configurations demonstrated significant enhancement of the GHS in the PT -symmetric system relative to the Hermitian case [71]. The pronounced enhancement of the GHS in the \mathcal{PT} -symmetric systems, resulting from precisely engineered gain and loss, underscores a distinct advantage over conventional Hermitian systems for applications necessitating substantial lateral shifts, such as quantum switching and high-precision microwave sensing. Our analysis provides valuable insights into the GHS in non-Hermitian CMM systems and may serve as a foundation for the development of microwave devices based on GHS effects.

ACKNOWLEDGEMENT

We acknowledge the financial support from the NSFC under grant No. 12174346.

REFERENCES

- [1] A A Serga, A V Chumak, and B Hillebrands, “YIG magnonics,” *J. Phys. D: Appl. Phys.* **43**, 264002 (2010).
- [2] B. Lenk, H. Ulrichs, F. Garbs, and M. Münzenberg, “The building blocks of magnonics,” *Phys. Rep.* **507**, 107 (2011).
- [3] Zeng-Xing Liu, Cai You, Bao Wang, Hao Xiong, and Ying Wu, “Phase-mediated magnon chaos-order transition in cavity optomagnonics,” *Opt. Lett.* **44**, 507 (2019).
- [4] Cui Kong, Hao Xiong, and Ying Wu, “Magnon-induced nonreciprocity based on the magnon Kerr effect,” *Phys. Rev. Appl.* **12**, 034001 (2019).
- [5] Xuan Zuo, Zhi-Yuan Fan, Hang Qian, Ming-Song Ding, Huatang Tan, Hao Xiong, and Jie Li, “Cavity magnomechanics: from classical to quantum,” *New J. Phys.* **26**, 031201 (2024).
- [6] M. F. Colombano, G. Arregui, F. Bonell, N. E. Capuj, E. Chavez-Angel, A. Pitanti, S. O. Valenzuela, C. M. Sotomayor-Torres, D. Navarro-Urrios, and M. V. Costache, “Ferromagnetic resonance assisted optomechanical magnetometer,” *Phys. Rev. Lett.* **125**, 147201 (2020).
- [7] Qian Zhang, Jie Wang, Tian-Xiang Lu, Ran Huang, Franco Nori, and Hui Jing, “Quantum weak force sensing with squeezed magnomechanics,” *Sci. China: Phys. Mech. Astron.* **67**, 100313 (2024).
- [8] Zhi-Yuan Fan, Liu Qiu, Simon Gröblacher, and Jie Li, “Microwave-optics entanglement via cavity optomagnonics,” *Laser Photonics Rev.* **17**, 2200866 (2023).
- [9] Bakht Hussain, Shahid Qamar, and Muhammad Irfan, “Entanglement enhancement in cavity magnomechanics by an optical parametric amplifier,” *Phys. Rev. A* **105**, 063704 (2022).
- [10] Jie Li, Yi-Pu Wang, Jian-Qiang You, and Shi-Yao Zhu, “Squeezing microwaves by magnetostriction,” *Natl. Sci. Rev.* **10**, nwac247 (2022).
- [11] Jie Li, Shi-Yao Zhu, and G. S. Agarwal, “Magnon-photon-phonon entanglement in cavity magnomechanics,” *Phys. Rev. Lett.* **121**, 203601 (2018).
- [12] Jie Li, Shi-Yao Zhu, and G. S. Agarwal, “Squeezed states of magnons and phonons in cavity magnomechanics,” *Phys. Rev. A* **99**, 021801 (2019).
- [13] Tian-Xiang Lu, Xing Xiao, Liu-Sha Chen, Qian Zhang, and Hui Jing, “Magnon-squeezing-enhanced slow light and second-order sideband in cavity magnomechanics,” *Phys. Rev. A* **107**, 063714 (2023).
- [14] Cui Kong, Bao Wang, Zeng-Xing Liu, Hao Xiong, and Ying Wu, “Magnetically controllable slow light based on magnetostrictive forces,” *Opt. Express* **27**, 5544 (2019).
- [15] Bijita Sarma, Thomas Busch, and Jason Twamley, “Cavity magnomechanical storage and retrieval of quantum states,” *New J. Phys.* **23**, 043041 (2021).
- [16] Shi-fan Qi and Jun Jing, “Magnon-assisted photon-phonon conversion in the presence of structured environments,” *Phys. Rev. A* **103**, 043704 (2021).

[17] Xufeng Zhang, Chang-Ling Zou, Liang Jiang, and Hong X. Tang, “Cavity magnomechanics,” *Sci. Adv.* **2**, e1501286 (2016).

[18] Rui-Chang Shen, Jie Li, Zhi-Yuan Fan, Yi-Pu Wang, and J. Q. You, “Mechanical bistability in kerr-modified cavity magnomechanics,” *Phys. Rev. Lett.* **129**, 123601 (2022).

[19] Guan-Ting Xu, Mai Zhang, Yu Wang, Zhen Shen, Guang-Can Guo, and Chun-Hua Dong, “Magnonic Frequency Comb in the Magnomechanical Resonator,” *Phys. Rev. Lett.* **131**, 243601 (2023).

[20] S. K. Özdemir, S. Rotter, F. Nori, and L. Yang, “Parity-time symmetry and exceptional points in photonics,” *Nat. Mater.* **18**, 783 (2019).

[21] Liang Feng, Ramy El-Ganainy, and Li Ge, “Non-Hermitian photonics based on parity-time symmetry,” *Nat. Photonics* **11**, 752 (2017).

[22] Ali Mostafazadeh, “Pseudo-hermiticity versus \mathcal{PT} symmetry: The necessary condition for the reality of the spectrum of a non-hermitian hamiltonian,” *J. Math. Phys.* **43**, 205 (2002).

[23] Ali Mostafazadeh, “Pseudo-Hermiticity versus \mathcal{PT} -symmetry. II. A complete characterization of non-Hermitian Hamiltonians with a real spectrum,” *J. Math. Phys.* **43**, 2814 (2002).

[24] Vladimir V. Konotop, Jianke Yang, and Dmitry A. Zezyulin, “Nonlinear waves in \mathcal{PT} -symmetric systems,” *Rev. Mod. Phys.* **88**, 035002 (2016).

[25] Wei Xiong, Zhuanxia Li, Yiling Song, Jiaoqiao Chen, Guo-Qiang Zhang, and Mingfeng Wang, “Higher-order exceptional point in a pseudo-Hermitian cavity optomechanical system,” *Phys. Rev. A* **104**, 063508 (2021).

[26] Guoqiang Zhang, Siyan Lin, Wei Feng, Yu Wang, Yang Yu, and Chuiping Yang, “Third-order exceptional surface in a pseudo-hermitian superconducting circuit,” *Sci. China Inf. Sci.* **68**, 180508 (2025).

[27] Carl M. Bender, Stefan Boettcher, and Peter N. Meisinger, “ \mathcal{PT} -symmetric quantum mechanics,” *J. Math. Phys.* **40**, 2201 (1999).

[28] Carl M. Bender and Stefan Boettcher, “Real Spectra in Non-Hermitian Hamiltonians Having \mathcal{PT} Symmetry,” *Phys. Rev. Lett.* **80**, 5243 (1998).

[29] Carl M. Bender, Bjorn K. Berntson, David Parker, and E. Samuel, “Observation of \mathcal{PT} phase transition in a simple mechanical system,” *Am. J. Phys.* **81**, 173 (2013).

[30] Yu-Long Liu, Rebing Wu, Jing Zhang, Şahin Kaya Özdemir, Lan Yang, Franco Nori, and Yu-xi Liu, “Controllable optical response by modifying the gain and loss of a mechanical resonator and cavity mode in an optomechanical system,” *Phys. Rev. A* **95**, 013843 (2017).

[31] Midya Parto, Yuzhou G. N. Liu, Babak Bahari, Mercedeh Khajavikhan, and Demetrios N. Christodoulides, “Non-hermitian and topological photonics: optics at an exceptional point,” *Nanophotonics* **10**, 403 (2021).

[32] H. Xu, D. Mason, Luyao Jiang, and J. G. E. Harris, “Topological energy transfer in an optomechanical system with exceptional points,” *Nature* **537**, 80 (2016).

[33] B. Peng, S. K. Özdemir, S. Rotter, H. Yilmaz, M. Liertzer, F. Monifi, C. M. Bender, F. Nori, and L. Yang, “Loss-induced suppression and revival of lasing,” *Science* **346**, 328 (2014).

[34] Weijian Chen, Şahin Kaya Özdemir, Guangming Zhao, Jan Wiersig, and Lan Yang, “Exceptional points enhance sensing in an optical microcavity,” *Nature* **548**, 192 (2017).

[35] William R. Sweeney, Chia Wei Hsu, Stefan Rotter, and A. Douglas Stone, “Perfectly absorbing exceptional points and chiral absorbers,” *Phys. Rev. Lett.* **122**, 093901 (2019).

[36] Changqing Wang, William R. Sweeney, A. Douglas Stone, and Lan Yang, “Coherent perfect absorption at an exceptional point,” *Science* **373**, 1261 (2021).

[37] Liang Feng, Zi Jing Wong, Ren-Min Ma, Yuan Wang, and Xiang Zhang, “Single-mode laser by parity-time symmetry breaking,” *Science* **346**, 972 (2014).

[38] Hossein Hodaei, Mohammad-Ali Miri, Matthias Heinrich, Demetrios N. Christodoulides, and Mercedeh Khajavikhan, “Parity-time-symmetric microring lasers,” *Science* **346**, 975 (2014).

[39] Lucas J. Fernández-Alcázar, Rodion Kononchuk, and Tsampikos Kottos, “Enhanced energy harvesting near exceptional points in systems with (pseudo-) \mathcal{PT} -symmetry,” *Commun. Phys.* **4**, 79 (2021).

[40] W D Heiss and G Wunner, “A model of three coupled wave guides and third order exceptional points,” *J. Phys. A* **49**, 495303 (2016).

[41] Guo-Qiang Zhang and J. Q. You, “Higher-order exceptional point in a cavity magnonics system,” *Phys. Rev. B* **99**, 054404 (2019).

[42] Gilles Demange and Eva-Maria Graefe, “Signatures of three coalescing eigenfunctions,” *J. Phys. A* **45**, 025303 (2011).

[43] Yi-Bing Qian, Ya-Ya Deng, Lei Tang, Deng-Gao Lai, and Bang-Pin Hou, “Phase-controlled higher-order exceptional points and nonreciprocal transmission in an optomechanical system,” *Phys. Rev. A* **111**, 033512 (2025).

[44] Hossein Hodaei, Absar U. Hassan, Steffen Wittek, Hipolito Garcia-Gracia, Ramy El-Ganainy, Demetrios N. Christodoulides, and Mercedeh Khajavikhan, “Enhanced sensitivity at higher-order exceptional points,” *Nature* **548**, 187 (2017).

[45] Chao Zeng, Kejia Zhu, Yong Sun, Guo Li, Zhiwei Guo, Jun Jiang, Yunhui Li, Haitao Jiang, Yaping Yang, and Hong Chen, “Ultra-sensitive passive wireless sensor exploiting high-order exceptional point for weakly coupling detection,” *New J. Phys.* **23**, 063008 (2021).

[46] Zin Lin, Adi Pick, Marko Lončar, and Alejandro W. Rodriguez, “Enhanced spontaneous emission at third-order dirac exceptional points in inverse-designed photonic crystals,” *Phys. Rev. Lett.* **117**, 107402 (2016).

[47] Zeng-Zhao Li, Weijian Chen, Maryam Abbasi, Kater W. Murch, and K. Birgitta Whaley, “Speeding Up Entanglement Generation by Proximity to Higher-Order Exceptional Points,” *Phys. Rev. Lett.* **131**, 100202 (2023).

[48] Kun Ding, Guancong Ma, Meng Xiao, Z. Q. Zhang, and C. T. Chan, “Emergence, coalescence, and topological properties of multiple exceptional points and their experimental realization,” *Phys. Rev. X* **6**, 021007 (2016).

[49] Pierre Delplace, Tsuneya Yoshida, and Yasuhiro Hatogai, “Symmetry-protected multifold exceptional points and their topological characterization,” *Phys. Rev. Lett.* **127**, 186602 (2021).

[50] Fei Wang and Chengdeng Gou, “Magnon-induced absorption via quantum interference,” *Opt. Lett.* **48**, 1164 (2023).

[51] Tao Shui, Wen-Xing Yang, Qingya Zhang, Xin Liu, and Ling Li, “Squeezing-induced giant Goos-Hänchen shift and hypersensitized displacement sensor in a two-level

atomic system,” *Phys. Rev. A* **99**, 013806 (2019).

[52] Ziauddin, You-Lin Chuang, and Ray-Kuang Lee, “Giant Goos-Hänchen shift using \mathcal{PT} symmetry,” *Phys. Rev. A* **92**, 013815 (2015).

[53] Saeed Asiri and Li-Gang Wang, “Controlling the Goos-Hänchen shift in a double prism structure using three-level Raman gain medium,” *Sci. Rep.* **13**, 22780 (2023).

[54] Ziauddin, Sajid Qamar, and M. Suhail Zubairy, “Coherent control of the Goos-Hänchen shift,” *Phys. Rev. A* **81**, 023821 (2010).

[55] Li-Gang Wang, Manzoor Ikram, and M. Suhail Zubairy, “Control of the Goos-Hänchen shift of a light beam via a coherent driving field,” *Phys. Rev. A* **77**, 023811 (2008).

[56] Rafi Ud Din, Muzamil Shah, Reza Asgari, and Gao Xianlong, “Impact of the Fizeau drag effect on Goos-Hänchen shifts in graphene,” *Phys. Rev. B* **109**, 115403 (2024).

[57] Johannes Picht, “Beitrag zur theorie der totalreflexion,” *Ann. Phys. (Leipzig)* **395**, 433 (1929).

[58] F. Goos and H. Hänchen, “Ein neuer und fundamentaler versuch zur totalreflexion,” *Ann. Phys. (Leipzig)* **436**, 333 (1947).

[59] F. Goos and Hilda Lindberg-Hänchen, “Neumessung des strahlversetzungseffektes bei totalreflexion,” *Ann. Phys. (Leipzig)* **440**, 251 (1949).

[60] Kurt Artmann, “Berechnung der seitenversetzung des totalreflektierten strahles,” *Ann. Phys. (Leipzig)* **437**, 87 (1948).

[61] Chun-Fang Li, “Negative lateral shift of a light beam transmitted through a dielectric slab and interaction of boundary effects,” *Phys. Rev. Lett.* **91**, 133903 (2003).

[62] Xuanbin Liu, Zhuangqi Cao, Pengfei Zhu, Qishun Shen, and Xiangmin Liu, “Large positive and negative lateral optical beam shift in prism-waveguide coupling system,” *Phys. Rev. E* **73**, 056617 (2006).

[63] Muhammad Idrees, Muhib Ullah, and Li-Gang Wang, “Enhancement of the Goos-Hänchen shift via chiral quantum-dot molecule systems,” *Phys. Rev. A* **108**, 013701 (2023).

[64] Muhib Ullah, Adeel Abbas, Jun Jing, and Li-Gang Wang, “Flexible manipulation of the Goos-Hänchen shift in a cavity optomechanical system,” *Phys. Rev. A* **100**, 063833 (2019).

[65] Anwar Ali Khan, Muqaddar Abbas, You-Lin Chaung, Iftikhar Ahmed, and Ziauddin, “Investigation of the Goos-Hänchen shift in an optomechanical cavity via quantum control,” *Phys. Rev. A* **102**, 053718 (2020).

[66] Q. Le Thien, R. Pynn, and G. Ortiz, “Entangled-Beam Reflectometry and Goos-Hänchen Shift,” *Phys. Rev. Lett.* **134**, 093802 (2025).

[67] Victor-O. de Haan, Jeroen Plomp, Theo M. Rekveldt, Wicher H. Kraan, Ad A. van Well, Robert M. Dalgliesh, and Sean Langridge, “Observation of the Goos-Hänchen shift with neutrons,” *Phys. Rev. Lett.* **104**, 010401 (2010).

[68] S. McKay, V. O. de Haan, J. Leiner, S. R. Parnell, R. M. Dalgliesh, P. Boeni, L. J. Bannenberg, Q. Le Thien, D. V. Baxter, G. Ortiz, and R. Pynn, “Observation of a giant goos-hänchen shift for matter waves,” *Phys. Rev. Lett.* **134**, 093803 (2025).

[69] Delian Lu, Ma Shanshan, Xiaojun Zhu, and Haixia Da, “Temperature controllable Goos-Hänchen shift and high reflectance of monolayer graphene induced by BK7 glass grating,” *Nanotechnology* **33**, 485201 (2022).

[70] Xianping Wang, Minghuang Sang, Wen Yuan, Yiyou Nie, and Haimei Luo, “Optical Relative Humidity Sensing Based on Oscillating Wave-Enhanced Goos-Hänchen Shift,” *IEEE Photon. Technol. Lett.* **28**, 264 (2016).

[71] Muhammad Waseem, Muhammad Irfan, and Shahid Qamar, “Magnomechanically controlled Goos-Hänchen shift in cavity QED,” *Phys. Rev. A* **110**, 033711 (2024).

[72] Nikhil Pramanik, K. C. Yellapragada, Suneel Singh, and P. Anantha Lakshmi, “Coherent control of Fano resonances in a macroscopic four-mirror cavity,” *Phys. Rev. A* **101**, 043802 (2020).

[73] Wenchao Ge, M. Al-Amri, Hyunchul Nha, and M. Suhail Zubairy, “Entanglement of movable mirrors in a correlated emission laser via cascade-driven coherence,” *Phys. Rev. A* **88**, 052301 (2013).

[74] Berihu Teklu, Tim Byrnes, and Faisal Shah Khan, “Cavity-induced mirror-mirror entanglement in a single-atom Raman laser,” *Phys. Rev. A* **97**, 023829 (2018).

[75] Shah Fahad, Muzamil Shah, and Gao Xianlong, “Photonic spin Hall effect in \mathcal{PT} -symmetric non-Hermitian cavity magnomechanics,” (2025), arXiv:2511.12173.

[76] Hao Xiong, LiuGang Si, XinYou Lv, XiaoXue Yang, and Ying Wu, “Review of cavity optomechanics in the weak-coupling regime: from linearization to intrinsic nonlinear interactions,” *Sci China Phys Mech Astron.* **58**, 1 (2015).

[77] Akhtar Munir, Muqaddar Abbas, Ziauddin, and Chunfang Wang, “Coherent- and dissipative-coupling control of photonic spin Hall effect in cavity magnomechanical system,” *Opt. Laser Technol.* **188**, 112813 (2025).

[78] Fujun Chen, “Electromagnetically induced grating in a nonlinear optomechanical cavity,” *Laser Phys. Lett.* **20**, 095206 (2023).

[79] Ling Li, Wenjie Nie, and Aixi Chen, “Transparency and tunable slow and fast light in a nonlinear optomechanical cavity,” *Sci. Rep.* **6**, 35090 (2016).

[80] D. F. Walls and G. J. Milburn, *Quantum Optics* (Springer-Verlag, Berlin, Heidelberg, 1994).

[81] Li-Gang Wang, Hong Chen, and Shi-Yao Zhu, “Large negative Goos-Hänchen shift from a weakly absorbing dielectric slab,” *Opt. Lett.* **30**, 2936 (2005).

[82] M. Harder, Y. Yang, B. M. Yao, C. H. Yu, J. W. Rao, Y. S. Gui, R. L. Stamps, and C.-M. Hu, “Level attraction due to dissipative magnon-photon coupling,” *Phys. Rev. Lett.* **121**, 137203 (2018).

[83] Tian-Xiang Lu, Huilai Zhang, Qian Zhang, and Hui Jing, “Exceptional-point-engineered cavity magnomechanics,” *Phys. Rev. A* **103**, 063708 (2021).

[84] X. Li, W. X. Yang, T. Shui, L. Li, X. Wang, and Z. Wu, “Phase control of the transmission in cavity magnomechanical system with magnon driving,” *J. Appl. Phys.* **128**, 235101 (2020).